論文 / 著書情報
Article / Book Information

Title	Near-threshold fatigue crack propagation in a Ni-based single crystal superalloy affected by crystallographic anisotropy
Authors	Putt Thanakun, Itsuki Sasakura, Keita Mase, Motoki Sakaguchi
Citation	Engineering Fracture Mechanics, Volume 309, , 110411
Pub. date	2024, 10
DOI	https://dx.doi.org/10.1016/j.engfracmech.2024.110411

Engineering Fracture Mechanics 309 (2024) 110411

Contents lists available at ScienceDirect

Engineering Fracture Mechanics

journal homepage: www.elsevier.com/locate/engfracmech

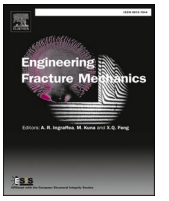

Near-threshold fatigue crack propagation in a Ni-based single crystal superalloy affected by crystallographic anisotropy

Putt Thanakun, Itsuki Sasakura, Keita Mase, Motoki Sakaguchi *

Department of Mechanical Engineering, Tokyo Institute of Technology, O-okayama 2-12-1, Meguro-ku, Tokyo, 152-8552, Japan

ARTICLE INFO

Keywords:
Ni-based single crystal superalloy
Crack propagation
Fatigue threshold
Crystal plasticity
Finite element analysis

ABSTRACT

Fatigue crack propagation in the near-threshold regime was investigated experimentally and numerically in a Ni-based single crystal superalloy, namely, CMSX-4. Fatigue crack propagation tests were conducted at room temperature using four types of specimens with different primary and secondary crystallographic orientations. The results reveal that the crystallographic orientations strongly affect the fatigue crack propagation behavior, including the crack paths, fatigue crack propagation rates, and fatigue threshold. Crystal plasticity finite element analysis was conducted to quantify the slip activity of an octahedral slip system in front of the crack tip, considering the actual 3D geometry of the crack plane and elastic–plastic anisotropy. The fatigue damage parameter, considering the slip activities of the individual octahedral slip systems, provides reasonable explanation for the fatigue crack propagation rates and crack paths in the near-threshold regime, regardless of the crystallographic orientation. Furthermore, these damage parameters are equivalent at the fatigue thresholds for all specimens with different crystallographic orientation.

1. Introduction

Ni-based superalloys are widely used to manufacture turbine blades in power generation and aircraft jet engines, owing to their superior resistance to creep, fatigue, and corrosive environments at high temperatures. In addition to centrifugal forces, turbine blades typically experience severe thermomechanical fatigue resulting from repeated start-up and shutdown cycles, leading to potential component failures [1]. Over the past few decades, numerous studies have attempted to elucidate fatigue behavior in superalloys to ensure their safe and reliable applications during service [2–16]. Among the significant fatigue parameters, the fatigue threshold, taken up by short crack propagation, plays a crucial role in structural design because a substantial portion of the component's life is spent in this region. The fatigue crack propagation behavior in the near-threshold regime has been reported to be highly sensitive to the material microstructure [17–19].

The traditional linear elastic fracture mechanics (LEFM) approach has been widely used to characterize fatigue crack propagation behavior. However, LEFM has certain limitations in quantifying short fatigue crack propagation, owing to its insufficient capability of capturing the local microstructure of the material. Conventional methodologies, such as the stress intensity factor and J-integral, have been applied to quantify macroscopic fatigue crack propagation, but these cannot indicate the local microscopic deformation mechanism at the crack tip within the length of the grain-scale.

* Corresponding author.
E-mail address: sakaguchi.m.ac@m.titech.ac.jp (M. Sakaguchi).

https://doi.org/10.1016/j.engfracmech.2024.110411
Received 20 March 2024; Received in revised form 15 August 2024; Accepted 17 August 2024
Available online 17 August 2024

The fatigue thresholds in Ni-based superalloys have been investigated by many previous studies [2,3,20–24]. As is known, many factors, such as the temperature, frequency, loading ratio, and microstructure, affect the fatigue threshold. For instance, King et al. [2,3] conducted an experiment to investigate the effect of temperature and grain size on a powder-formed Ni-based superalloy. Mercer et al. [4] investigated the micro-mechanisms of fatigue crack propagation in the forged polycrystalline IN718 Ni-based superalloy under various loading conditions, using the scanning electron microscope (SEM) and transmission electron microscope (TEM). Their results revealed that fatigue crack propagation progressed with a transgranular crystallographic mode of fracture in near-threshold regimes. Sengupta et al. [20,21] employed a single crystal Ni-based superalloy, CMSX-4, to investigate the influence of the size and distribution of γ' precipitates on the near-threshold fatigue crack propagation rate and fatigue threshold at room temperature and 650 °C. The above-mentioned studies also considered the effect of the loading ratio applied to compact tension specimens with [0 0 1] orientation in the loading direction. Although many studies have investigated fatigue crack propagation behavior in Ni-based superalloys, the influence of crystallographic orientation in this anisotropic material, particularly regarding the microscopic deformation mechanism at the crack tip, remains unclear.

To quantify the fatigue threshold accurately, the local microscopic deformation mechanism near the crack tip should be carefully considered. Here, the rate of growth and the crack path for near-threshold loading depend on the microstructure. Consequently, any quantitative method must capture both the rate and the path. Recent studies have proposed various crack driving forces or fatigue damage parameters, with consideration of both the rate and path for the near-threshold regime and the microstructure of the material. For example, Wan et al. [25] introduced a microstructure-sensitive driving force, namely, the stored energy density, which is based on the idea that the local slip under fatigue gives rise to dislocation interaction. This stored energy density, determined by the dislocation density, was used for the prediction of cycles up to fatigue crack nucleation in polycrystal ferritic steel. Furthermore, this parameter has been used to rationalize various fatigue crack propagation behaviors [13,15,26–28]. For instance, Karamitros et al. [26] investigate the mechanistic short crack growth in single crystal Ni $\gamma - \gamma'$ microstructure using crystal plasticity and eXtended finite element method based on the stored energy density. Their model offered satisfactory prediction of both the crystallographic crack paths and the rate of growth in the $\gamma - \gamma'$ microstructure. Even though many crack driving forces or fatigue damage parameters have been previously introduced, they have not been used to quantify the fatigue threshold in single crystal Ni-based superalloys, considering the influence of crystallographic orientations. Additionally, various studies have confirmed that the grain properties and crystallographic orientations strongly affect the fatigue behavior and fatigue crack initiation. Previous studies by the authors [12,16] have shown that crystal plasticity finite element (CPFE) analysis considering the actual geometry of a crystallographic crack can provide a reasonable explanation for the effect of crystallographic orientation on the fatigue crack propagation paths and rates in a single crystal Ni-based superalloy.

In this study, fatigue tests were conducted to investigate the influence of the crystallographic orientations on fatigue crack propagation behavior and the micro-mechanisms in the near-threshold regime. Here, a single crystal Ni-based superalloy with different crystallographic orientations was employed to eliminate the effect of grain boundaries, which aids the examination of in-grain deformation mechanisms. Additionally, local fatigue damages were analyzed and compared using CPFE analysis, which considers the elastic anisotropy of the material and localized slip deformation.

2. Experimental procedure

2.1. Material and specimen preparation

The material employed in this study is a second-generation single crystal Ni-based superalloy, CMSX-4. The chemical composition of this material is 9.7Co–6.5Cr–6.4 W–5.7Al–1.0Ti–6.6Ta–0.6Mo–3.0Re–Bal Ni (wt.%). For this material, heat treatments were conducted as follows: solution treatments at 1277 °C for 2 h, 1288 °C for 2 h, 1296 °C for 3 h, 1304 °C for 3 h, 1313 °C for 2 h, 1316 °C for 2 h, and 1277 °C for 2 h followed by aging treatments at 1140 °C for 6 h and 871 °C for 20 h. Fig. 1 shows the microstructure after the heat treatments, which consists of the γ phase (matrix phase) and cuboidal γ' phase (precipitate phase). The average size of the cuboidal precipitate phase was approximately 0.42 μm, and the volume fraction of the precipitate phase was approximately 66 %.

Compact (C(T)) specimens were cut from cast ingots of this single crystal material using wire electric discharge machining techniques. The geometry of the C(T) specimens is shown in Fig. 2. The surfaces were polished with several grades of emery papers up to #2000. Buff polishing was additionally performed on both sides for microscopic observations. Four types of C(T) specimens were prepared by changing the combination of the primary (loading direction) and secondary (crack propagation direction) orientations. Fig. 3 shows these four types of specimens including the ⟨100⟩⟨100⟩, ⟨100⟩⟨110⟩, ⟨110⟩⟨100⟩, and ⟨110⟩⟨110⟩ specimens. The corresponding configurations of the octahedral slip planes are also shown, and the types of the {1 1 1} slip planes are indicated by four different colors. Here, the first and second Miller indices for the specimens are the primary and secondary orientations, respectively. This rule for the Miller indices is identical to that in previous studies [4,8,14,16,29]. For example, the ⟨110⟩⟨100⟩ specimen has its loading direction along the ⟨110⟩ crystallographic orientation and its crack propagation direction along the ⟨100⟩ orientation.

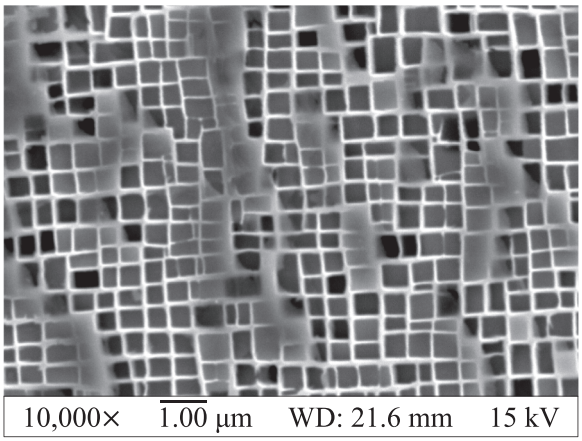

Fig. 1. γ/γ' microstructure after heat treatment.

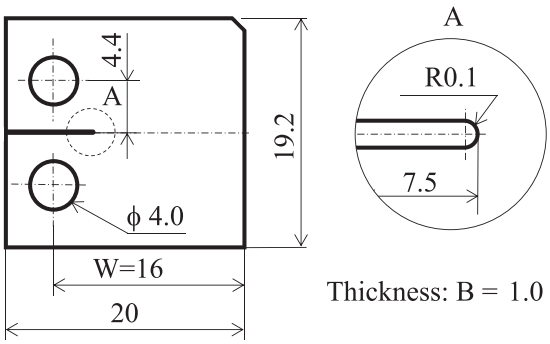

Fig. 2. Geometry of specimens employed in this study (mm).

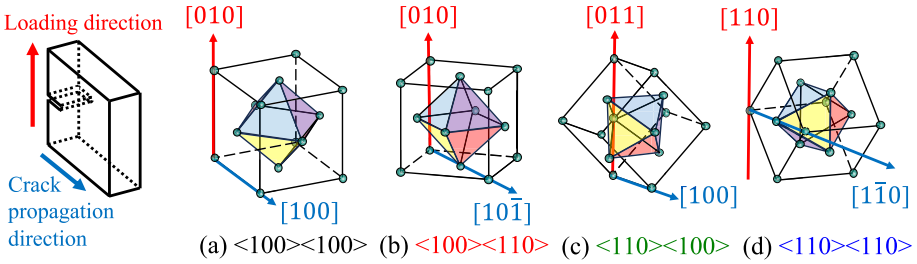

Fig. 3. Schematic illustration of octahedral slip planes in four C(T) specimen types.

2.2. Fatigue crack propagation test

Fatigue crack propagation tests were performed at room temperature using an electro-hydraulic machine. During the tests, the front and back surfaces of the specimen were observed using two digital microscopes (KEYENCE VHX-5000 and KEYENCE VH-5500SP) to identify the slip deformation and measure the crack length. Sine wave loading was applied. The loading ratio was set to 0.4 and loading frequency was 10 Hz. Conventional tests of ΔK_I decreasing and ΔK_I increasing were carried out in accordance with ASTM E647 [30]. Here, ΔK_I is given as follows:

$$\Delta K_I = \frac{\Delta P}{B\sqrt{W}} \frac{2+\xi}{(1-\xi)^{3/2}} \left(0.886 + 4.64\xi - 13.32\xi^2 + 14.72\xi^3 - 5.6\xi^4\right) \tag{1}$$

where ξ equals a/W; ΔP, B, W, and a are the loading range, specimen thickness, specimen width, and projected crack length, respectively. A pre-crack with a length of 1.0 mm was introduced at room temperature before the test to eliminate the influence of the initial notch. For the ΔK_I increasing test, the applied loading was kept constant since the beginning of the test. A single test was conducted for each specimen type, and the initial ΔK_I was 11 MPa·m$^{1/2}$ for ⟨100⟩⟨110⟩ and 13 MPa·m$^{1/2}$ for the remaining specimens. For the ΔK_I decreasing test, compliance for the ΔK_I decreasing test was set to be constant at –0.08 mm^{-1}. A single test was conducted for the ⟨100⟩⟨110⟩, ⟨110⟩⟨100⟩, and ⟨110⟩⟨110⟩ specimens, and the initial ΔK_I values were 11, 13.2, and 13 MPa·m$^{1/2}$, respectively. Moreover, two tests were conducted for the ⟨100⟩⟨100⟩ specimen, and the initial ΔK_I values were 10.8 MPa·m$^{1/2}$ and 12 MPa·m$^{1/2}$. To calculate the fatigue threshold ΔK_{th}, the best-fit linear line was determined using a minimum of five data points in the crack propagation rate range of the 10^{-10}–10^{-9} m/cycle in the log da/dN versus log ΔK. The fatigue threshold can be calculated from the ΔK value that corresponds to the crack propagation rate of 10^{-10} m/cycle using the fitted line.

3. Experimental results

3.1. Fatigue crack propagation path and fracture surface

Fig. 4 shows the crack propagation paths, fracture surfaces, and corresponding 3D schematic illustrations for the specimens in the ΔK_I decreasing test. In the 3D illustrations, the Mode I crack planes are gray, while the crystallographic crack planes are blue, purple, red, and yellow, according to the schematic illustrations in Fig. 3.

As shown in Fig. 4(a), the fatigue crack in the ⟨100⟩⟨100⟩ specimen propagated mainly along the blue slip plane at an inclination angle of 45° to both the crack propagation and specimen thickness direction. This was a mixed-mode crack encompassing Mode I, II, and III propagation. Additionally, the fatigue crack periodically deflected onto the red slip plane, particularly the backside of the specimen (upper part of the fracture surface, as shown in Fig. 4(a)). For the ⟨100⟩⟨110⟩ specimen, the fatigue crack propagated only along the blue slip plane with Mode I and III propagation, as shown in Fig. 4(b). The blue slip plane in this specimen was parallel to the crack propagation direction and inclined at 55° to the thickness direction. In the ⟨110⟩⟨100⟩ specimen in Fig. 4(c), the fatigue crack only exhibited Mode I propagation, without propagating along any slip plane. For the ⟨110⟩⟨110⟩ specimen, the fatigue crack primarily propagated on the blue slip plane exhibiting Mode I and III propagation, particularly when ΔK_I was lower than 12 MPa·m$^{1/2}$. The blue slip plane in this specimen was parallel to the propagation direction and inclined at 35° to the thickness direction. The fatigue crack periodically deflected onto the yellow and red slip planes, which were perpendicular to the propagation direction. Note that the blue-colored line, representing the crack path observed on the back of the specimen, in the area outside the available specimen image is marked as a dotted line. Notably, the above-mentioned fatigue crack propagation behaviors of the four specimen types were similar in the ΔK_I increasing test, which is also identical to the findings from a previous study by the authors using CMSX-4 [9].

Closed SEM observation of the crack planes was carried out for the ⟨110⟩⟨110⟩ and ⟨110⟩⟨100⟩ specimens. The former specimen is a typical example of crystallographic cracking, while the latter exhibits opening mode cracking. Fig. 5 shows the microstructures and schematic illustrations of the crack plane observed in the ⟨110⟩⟨110⟩ and ⟨110⟩⟨100⟩ specimens. During crystallographic cracking (Fig. 5(a)), both the γ and cuboidal γ′ phase were sheared along the {1 1 1} slip planes, resulting in a triangular γ′ phase in the SEM image. Contrary to the ⟨110⟩⟨100⟩ specimen, the crack plane observed in the macroscopic scale is flat and perpendicular to the loading direction, indicating Mode I cracking as shown in Fig. 4(c). However, when observing the crack plane at microscopic scale using SEM, some local slip deformations can be observed, as shown in Fig. 5(b). These local slip deformations may indicate multiple slip mechanisms, which lead to Mode I cracking at the macroscopic scale [31]. As shown in Fig. 5(b), multiple shapes of the cuboidal γ′ phase can be observed, owing to different local slip deformation as shown in the schematic illustrations, where slip deformation along the blue and yellow planes is given as an example. In this scenario, the triangular γ′ phase formed within the crack plane because of shearing along the blue slip plane, while the “inclined line” (indicated by red arrows) resulted from shearing along the yellow slip plane. This indicates that although the crack propagated in the Mode I manner macroscopically, some local slip deformations and the shearing mode cracking can be partially observed. However, most of the area in SEM image (Fig. 5(b)) shows the rectangular shape cuboidal γ′ phase. There are two possible causes that lead to the rectangular γ′ phase in the SEM image, including (1) crack propagation along the interface between the γ and γ′ phases, and (2) crack propagation along the cubic slip systems through the γ′ phase. It is known that the slip deformation in the Ni-based superalloy, which exhibits an FCC structure, predominantly occur along the octahedral slip system at a temperature of 26–427 °C, while the cubic slip system becomes active at 427 °C and higher [5]. This study focused on the fatigue crack behavior at room temperature; thus, the rectangular γ′ phase indicates the presence of the non-sheared cuboidal γ′ phase, as indicated by the gray color in the schematic illustrations in Fig. 5(b), where the crack propagated in the Mode I manner probably through the interface between the γ and γ′ phase.

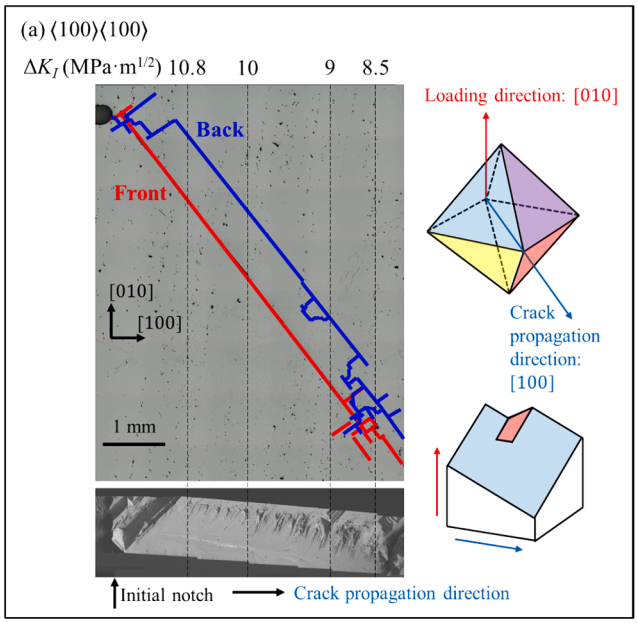

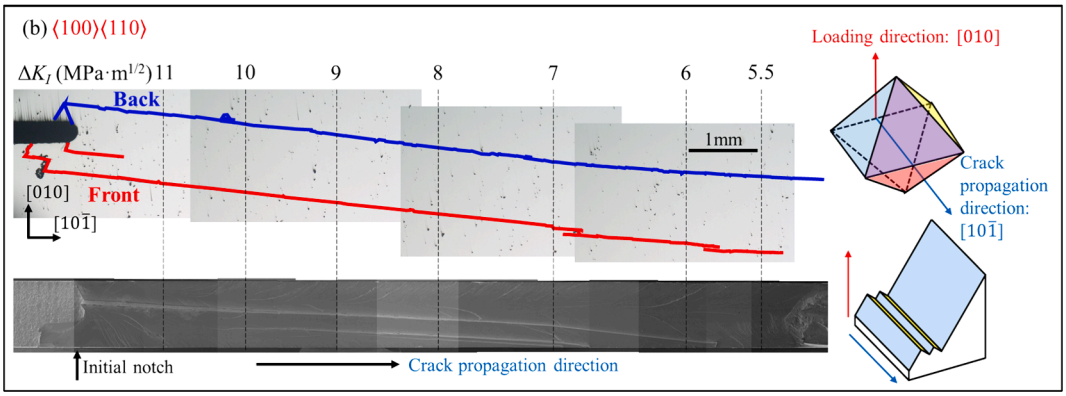

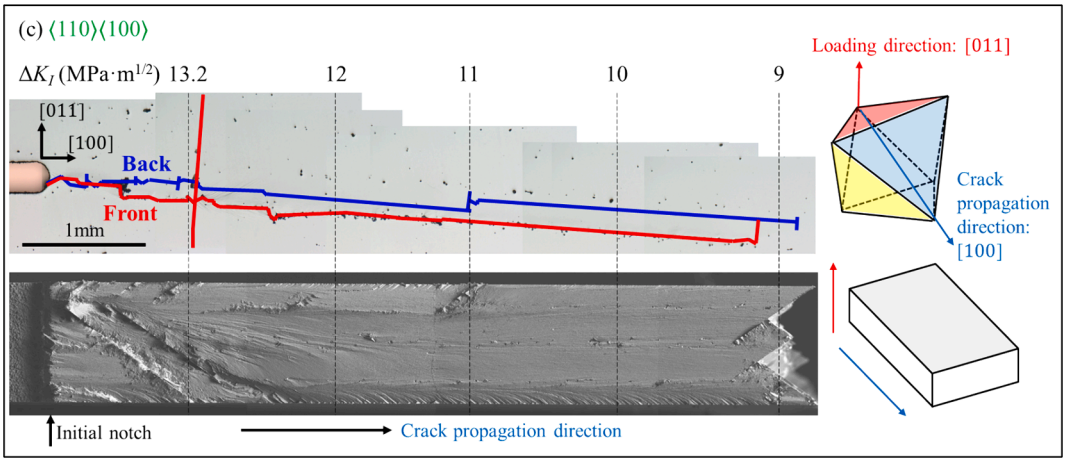

Fig. 4. Crack paths and fracture surfaces in four specimen types: (a) ⟨100⟩⟨100⟩; (b) ⟨100⟩⟨110⟩; (c) ⟨110⟩⟨100⟩; (d) ⟨110⟩⟨110⟩ (red lines and blue lines indicate the crack path observed on the front surfaces and back surfaces, respectively). (For interpretation of the references to color in this figure legend, the reader is referred to the web version of this article.)

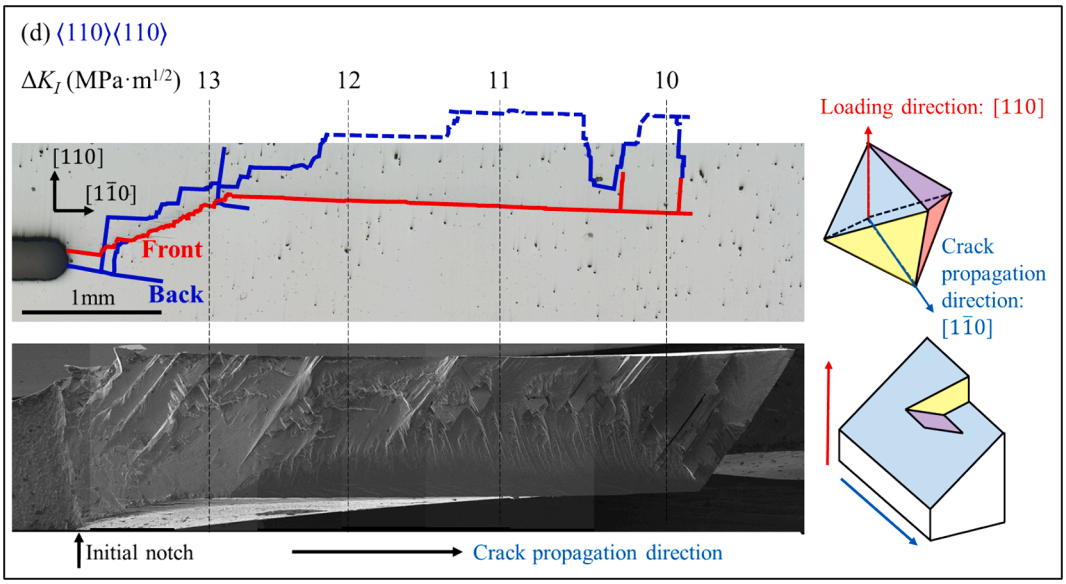

Fig. 4. (*continued*).

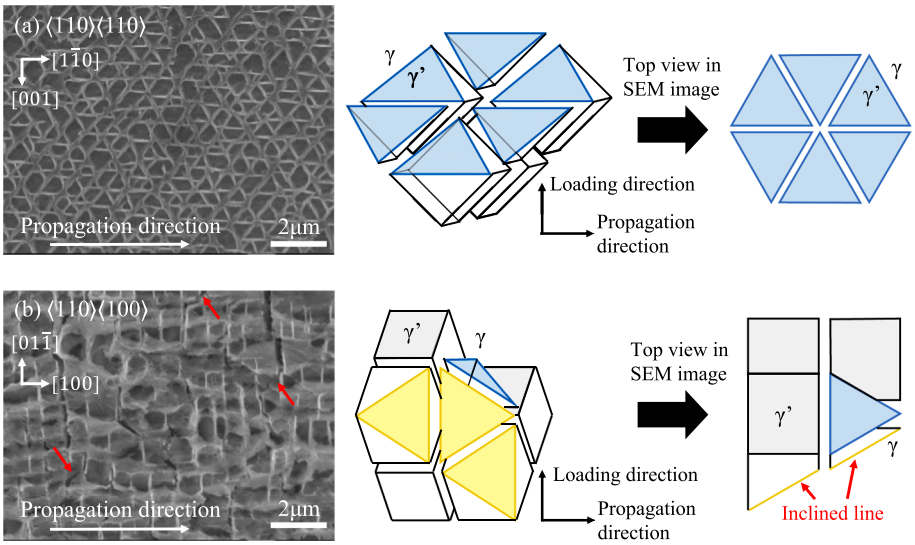

Fig. 5. Microstructure of fracture surface: (a) ⟨110⟩⟨110⟩ specimen (crystallographic crack surface); (b) ⟨110⟩⟨100⟩ specimen (Mode I crack surface). The schematic illustrations show the sheared cuboidal γ′ phases and their top view.

3.2. Fatigue crack propagation rate

Fig. 6 summarizes the crack propagation rate *da/dN* of the four types of specimens as a function of ΔK_I. Here, *da/dN* and ΔK_I were calculated based on the projected crack length. Data plots are distinguished by solid and open symbols for the ΔK_I decreasing test and ΔK_I increasing test, respectively. Here, the best-fit linear lines for each specimen, which are determined using at least five data points in the crack propagation rate range of 10^{-10}–10^{-9} m/cycle, are inserted into the plot. The calculated ΔK_{th} values are 7.67, 4.95, 8.71, and 9.57 MPa·m$^{1/2}$ for the ⟨100⟩⟨100⟩, ⟨100⟩⟨110⟩, ⟨110⟩⟨100⟩, and ⟨110⟩⟨110⟩ specimen, respectively. The comparison of *da/dN* in the ΔK_I increasing test (open symbols) shows that the ⟨100⟩⟨110⟩ specimen exhibits the highest rate, followed in sequence by the ⟨100⟩⟨100⟩, ⟨110⟩⟨110⟩, and ⟨110⟩⟨100⟩ specimens. This order is the same as the results obtained by the ΔK_I increasing test in a previous study by the authors [9]. Moreover, the order of *da/dN* from the ΔK_I decreasing test (solid symbols) is the ⟨100⟩⟨110⟩, ⟨100⟩⟨100⟩, ⟨110⟩⟨100⟩, and ⟨110⟩⟨110⟩ specimen. In the ⟨110⟩⟨110⟩ specimen, the crack propagated along multiple slip planes unlike the ⟨100⟩⟨100⟩ and ⟨100⟩⟨110⟩ specimens, which propagated along a single slip plane in a shearing manner. The multiple crack tips could be observed in the ⟨110⟩⟨110⟩ specimen, which may have led to crack retardation because the multiple crack tips can cause the

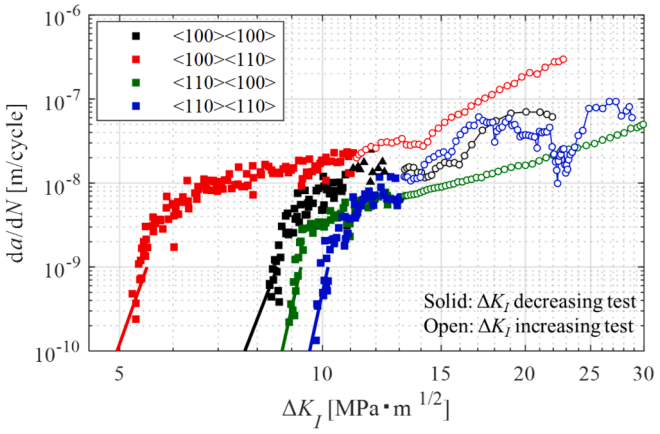

Fig. 6. Crack propagation rate in four specimen types as a function of Mode I stress intensity factor range ΔK_I.

stress relaxation in the vicinity of the primary crack tip, resulting in a decrease in the crack propagation rate as well as an increase in the value of the ΔK_{th} [32,33]. Notably, although an intrinsic resistance to crystallographic cracking in the ⟨100⟩⟨100⟩, ⟨100⟩⟨110⟩, and ⟨110⟩⟨110⟩ specimens should be the same relevant to the sliding and decohesion of the {1 1 1} slip planes, the ΔK_{th} values are strongly influenced by the crystallographic anisotropy of the C(T) specimen.

In Fig. 6, the ΔK_I could not sort the fatigue crack propagation rates in the four types of specimens with different crystallographic orientations. This is possibly because the ΔK_I only considers the Mode I cracking without considering the contribution of the Mode II and Mode III cracking. It is thus necessary to evaluate the contribution of the Mode II and Mode III cracking to sort the fatigue crack propagation rates. Here, the parameter called shear stress intensity factor range, ΔK_τ, which was proposed by Sakaguchi et al. [34], considering both the contribution of the Mode II and Mode III, was employed to elucidate the contribution of the shear stress component on the actual geometry of the {1 1 1} slip planes. This parameter was proposed to elucidate the shear-dominant fatigue crack propagation in the single crystal Ni-base superalloy, and it could satisfactorily sort the fatigue crack propagation rate regardless of the crystallographic orientations [34]. The ΔK_τ is given as follows:

$$\Delta K_\tau = F_\tau(\xi)\Delta\tau\sqrt{\pi a'} \tag{2}$$

$$F_\tau(\xi) = \sqrt{\frac{2}{\pi\xi}\tan\left(\frac{\pi\xi}{2}\right)} \tag{3}$$

$$\tau = \sigma_\infty \cos\phi \sin\phi \tag{4}$$

$$\sigma_\infty = \frac{6Pa}{BW^2} \tag{5}$$

where ϕ is an angle between the slip plane normal and the loading axis; a is the projected crack length; a' is an actual crack length. Note that τ is not the resolved shear stress, but a maximum shear stress on the slip plane. In order to evaluate the fatigue crack propagation rate for the crystallographic cracking, the actual crack length should be considered rather than the projected crack length. Here, the 3D crack length is given as follows:

$$A = \frac{a}{\cos\theta\cos\eta} \tag{6}$$

where θ and η are angles representing the 3D crack plane.

The relationship between dA/dN and ΔK_τ is given in Fig. 7. Data plots are distinguished by solid and open symbols for the ΔK_I decreasing test and ΔK_I increasing test, respectively. Note that the results of the ⟨110⟩⟨100⟩ specimen are not included because the fatigue crack exhibited Mode I propagation without the contribution of the shearing component in the macroscopic scale. It is found in Fig. 7 that the ⟨100⟩⟨100⟩ and ⟨110⟩⟨110⟩ specimens show almost comparable threshold level based on the dA/dN and ΔK_τ relationship. Nevertheless, the dA/dN in the ⟨100⟩⟨110⟩ specimen still exhibits the highest propagation rate, and the smallest threshold level. This can be concluded that even though the fatigue crack propagation rate in the ⟨100⟩⟨100⟩ and ⟨110⟩⟨110⟩ specimens could be sorted into a single trendline by using the parameter ΔK_τ, this parameter still could not arrange all four specimens together. In addition, any combination of ΔK_I and ΔK_τ will not make the data align in a single trendline as the fatigue crack propagation behavior in the three types of specimens are not so different when sorting by ΔK_I and ΔK_τ. This indicates that rather than using the ΔK_I and/or ΔK_τ to rationalize the mixed-mode cracking, it is preferable to consider, for example, shear strain or the activation of each slip system individually, to quantify the fatigue crack propagation rate regardless of the crystallographic orientations.

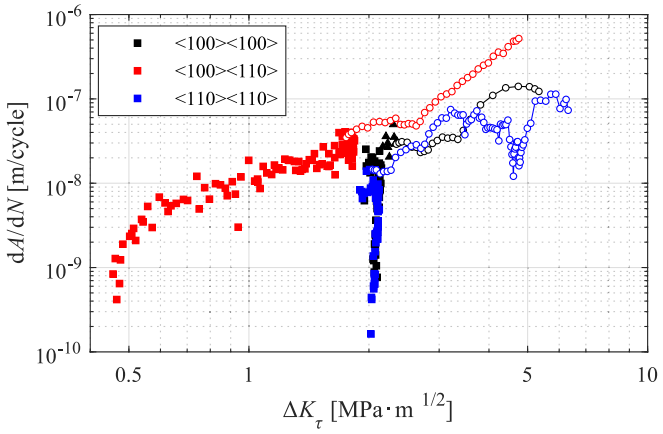

Fig. 7. Crack propagation rate in three specimen types as a function of shear stress intensity factor range ΔK_τ.

4. Crystal plasticity analysis

Fatigue crack propagation along the crystallographic plane involves localized plastic deformation in persistent slip bands. Hence, the plastic strain generated near the crack tip during cyclic loading has been considered to interpret fatigue damage [25,32,33]. In face-centered cubic (FCC) materials, including single crystal Ni-based superalloys, plastic deformation is primarily associated with dislocation motion along the octahedral slip system. Plastic deformation is recognized as slip, that is, plastic shear strain along each slip system.

For the precise evaluation of anisotropic plastic deformation in a single crystal material, the activity of each slip system should be quantified. Here, finite element analysis incorporating crystal plasticity theory can provide the most appropriate assessment, because CPFE can consider several important factors, including the (1) elastic anisotropy, (2) 3D geometry of the crack tip, and (3) localized slip deformation at the crack tip. The authors have previously demonstrated that CPFE analysis considering the actual 3D geometry of the crystallographic crack can provide a reasonable explanation for the effect of the crystallographic orientation on the cracking path and propagation rate in a single crystal Ni-based superalloy [4,8,16,29]. A similar analytical framework was applied in this study to quantify the localized slip deformation during near-threshold fatigue crack propagation.

4.1. Crystal plasticity theory

The single crystal Ni-based superalloy exhibits an FCC structure that includes four types of {1 1 1} slip planes and 12 slip systems, as shown in Fig. 8. Here, the blue, purple, red, and yellow slip planes correspond to slip planes 1, 2, 3, and 4, respectively. The slip planes and slip directions are defined in the local coordinate system, which is established with the *X*-, *Y*-, and *Z*-axis in the [1 0 0], [0 1 0], and [0 0 1] direction, respectively. The global coordinate system, which is kept the same under different crystallographic orientations, is the reference for the rotation of the defined local coordinate system. Here, the *X*-, *Y*-, and *Z*-axis are defined as the crack propagation, loading, and thickness directions, respectively. The crystallographic orientations can be achieved by rotating the crystal in the global coordinate system in the local coordinate system. For example, the ⟨110⟩⟨100⟩ specimen can be achieved by rotating the crystal around the *X*-axis by −45°.

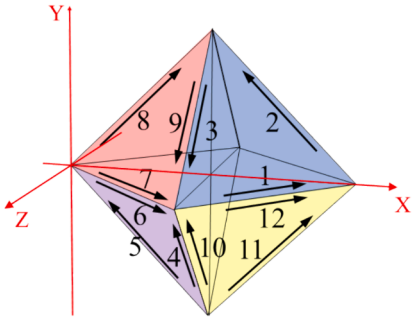

Slip systems	Slip planes	Slip directions
1	Plane 1: (111)	[10$\bar{1}$]
2		[$\bar{1}$10]
3		[0$\bar{1}$1]
4	Plane 2: ($\bar{1}\bar{1}$1)	[011]
5		[$\bar{1}$10]
6		[101]
7	Plane 3: ($\bar{1}$11)	[101]
8		[110]
9		[0$\bar{1}$1]
10	Plane 4: (1$\bar{1}$1)	[011]
11		[110]
12		[10$\bar{1}$]

Fig. 8. Slip planes and slip systems in FCC crystal structure.

The crystal plasticity theory employed in this study is based on the theoretical framework of Asaro [35]. The constitutive equation is given as follows:

$$\overset{\nabla}{\sigma} = \mathbf{C} : \mathbf{D} - \sum_{k=1}^{n} \left(\mathbf{C} : \mathbf{P}^{k} + \mathbf{W}^{k} \cdot \sigma - \sigma \cdot \mathbf{W}^{k}\right)\dot{\gamma}^{k} \tag{7}$$

Here, $\overset{\nabla}{\sigma}$ is the Jaumann rate of the Cauchy stress, σ is the stress, $\mathbf{C}$ is a tensor of the elastic moduli, and $\mathbf{D}$ is the deformation rate tensor; $\mathbf{P}^{k}$ and $\mathbf{W}^{k}$ are the stretching and spin tensors, respectively, for a slip system k such that the following relationships hold:

$$\mathbf{P}^{k} = \frac{1}{2}\left(\mathbf{n}^{k} \otimes \mathbf{b}^{k} + \mathbf{b}^{k} \otimes \mathbf{n}^{k}\right) \tag{8}$$

$$\mathbf{W}^{k} = \frac{1}{2}\left(\mathbf{n}^{k} \otimes \mathbf{b}^{k} - \mathbf{b}^{k} \otimes \mathbf{n}^{k}\right) \tag{9}$$

Here, $\mathbf{n}^{k}$ and $\mathbf{b}^{k}$ are the unit directi on vectors of the slip plane normal and slip direction, respectively; $\dot{\gamma}^{k}$ in Eq. (7) is the shear strain rate of a slip system k, which is given by the following kinetic law:

$$\dot{\gamma}^{k} = \dot{\gamma}_{0}\mathrm{sgn}\left(\frac{\tau^{k}}{\tau_{0}}\right)\left|\frac{\tau^{k}}{\tau_{0}}\right|^{1/m} \tag{10}$$

where τ^{k} is the resolved shear stress along the slip system k; $\dot{\gamma}_{0}$ and τ_{0} are the reference shear strain rate and yield shear stress, respectively; m is a rate-dependent parameter. These constitutive equations were incorporated into Abaqus for implicit analysis with the user-defined material subroutine UMAT for single crystal plasticity. The material parameters m, τ_{0}, and $\dot{\gamma}_{0}$ were set to $m = 0.01$, $\tau_{0} = 360$ MPa, and $\dot{\gamma}_{0} = 1 \times 10^{-5}$ to reproduce the stress–strain relationship in the tensile test at room temperature. Because the single crystal Ni-based superalloy exhibits elastic–perfectly-plastic behavior at room temperature [36], the strain hardening of the slip systems was not considered.

4.2. Crystal plasticity finite element model

4.2.1. Finite element model

Finite element (FE) models were established for all four types of specimens by following the specimen geometry and actual fracture surfaces shown in Fig. 4. Fig. 9 shows the FE models for all specimens, and mesh around the crack tip is also given. For the ⟨100⟩⟨100⟩, ⟨100⟩⟨110⟩, and ⟨110⟩⟨110⟩ specimen, cracks mainly propagated along slip plane 1; therefore, the crack geometries in the FE models were designed to have the same inclination as slip plane 1. For the ⟨110⟩⟨100⟩ model with the Mode I crack, a curved crack tip was introduced and was confirmed to affect the stress and strain fields around the crack tip, particularly in Mode I cracking [37]. To optimize the time and cost of analysis, only a half of the specimen was modeled for the ⟨110⟩⟨100⟩ specimen because of symmetry, while the entire specimen was modeled for the other specimens. The projected crack lengths were fixed at $a/W = 0.4$ for all models. The models consisted of approximately 40,000 elements and 200,000 nodes. The minimum mesh size in the vicinity of the crack tip was set to be 5 μm, which was confirmed to be sufficiently fine for stable calculations based on convergence and sensitivity studies. The C3D20R element type was used to ensure the high precision of the calculation results. An external load was applied by a point force to the reference point at the center of the loading hole, simulating the maximum load in the experiments. The displacement in the horizontal direction of this reference point was constrained, and the distance between the reference point and the upper half surface of the loading hole was kept constant to allow the rotation of the specimen during loading. The anisotropic elastic moduli for CMSX-4 at room temperature were set to $C_{11} = 248.8$ GPa, $C_{12} = 158.5$ GPa, and $C_{44} = 129.8$ GPa, according to Siebörger et al. [38]. The crystallographic orientation of the models was defined by setting the axis directions of the global and local coordinate systems.

4.2.2. Damage parameter for crystallographic cracking

In the case of the shearing mode cracking, the critical plane approach is suitable for assessing fatigue life [39]. This method focuses on fatigue damage on a specific plane, assuming that crack initiation and propagation occur on the plane where certain damage reaches its maximum. The fatigue damage parameter proposed in the previous study [11] was adopted in this study. This parameter can evaluate the fatigue damage on each slip plane by considering the activation of each slip system individually, as follows:

$$F^{i} = \int \gamma^{j}_{SPA}\left(1 + \eta\frac{\sigma^{i}_{n}}{\sigma_{y}}\right)dr \ , \ i = 1, 2, 3, 4, \tag{11}$$

$$\gamma^{i}_{SPA} = \left|\sum_{j=3i-2}^{3i} \gamma^{j}\mathbf{b}^{j}\right| \tag{12}$$

where F^{i} is the fatigue damage on slip plane i; σ^{i}_{n} is the normal stress on slip plane i normalized by the yield stress σ_{y}; η is a constant representing the contribution of normal stress on crack propagation; γ^{j} and $\mathbf{b}^{j}$ are the corresponding plastic shear strain and Burgers vector on slip plane i; γ^{i}_{SPA} is the total slip on slip plane i, which is called slip plane activity, and is an absolute value of the summation of

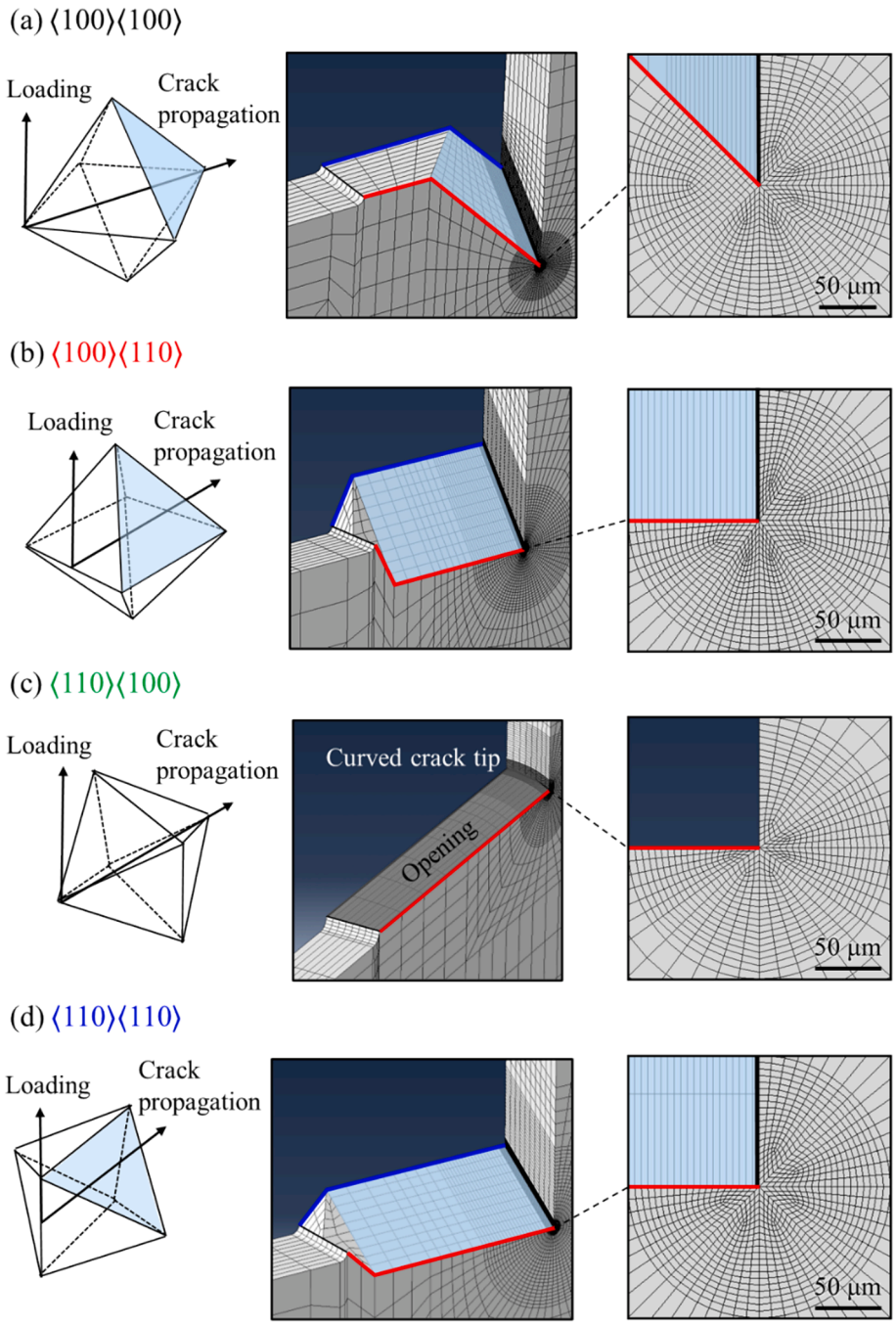

Fig. 9. Finite element models reproducing crystallographic cracking for specimens: (a) ⟨100⟩⟨100⟩, (b) ⟨100⟩⟨110⟩, (c) ⟨110⟩⟨100⟩, and (d) ⟨110⟩⟨110⟩.

the plastic shear strains along the three slip directions; F can be calculated by integrating γ^{i}_{SPA} along the distance from the crack tip r in the slip plane direction. Three concepts are considered in this damage parameter [11]: (1) three slip systems exist on each slip plane and the crack does not always propagate along a specific ⟨110⟩ slip direction [40]; therefore, all three slips should be considered to evaluate the fatigue damage on each slip plane. (2) In crystallographic cracking, the crack propagates along a certain slip plane; therefore, the damage should be evaluated by considering the accumulation of slip in the specific slip plane. (3) The resolved shear stress acting on the slip plane drives the plastic deformation that enhances the decohesion of slip planes, while the normal stress separates the planes; the normal stress contribution is weighted by parameter η. Previous studies by the authors [4,16] have shown that η does not significantly affect the general trend of F; therefore, η is considered as 0.5. According to the critical plane approach [39], it is

assumed that the crack will propagate on the slip plane with the highest F among all the {1 1 1} slip planes. Note that the slip plane activity in Eq. (11) is not a plastic shear strain range in the cyclic stress–strain hysteresis loop, but it is the strain at the maximum loading. The simulation of fatigue crack propagation should normally consider the cyclic plastic strain range, not the strain at maximum loading; however, the simulation of full loading cycles requires more time and cost. Thus, this study only considered the fatigue damage F from the loading up to the maximum load, which could help simplify the analysis. It has been confirmed through several models that the damage parameter F is positively correlated with plastic shear strain range in the stress–strain hysteresis loop. Although the damage parameter F might not capture all the complexities of crack tip mechanics, it could simplify the representation of complex mechanics, making it easier to implement in computational models.

Fig. 10 shows the computed results of the slip plane activity γ^i_{SPA} in the ⟨100⟩⟨100⟩ model when $\Delta K_I = 10$ MPa·m$^{1/2}$, which are plotted as a function of the distance from the crack tip r and the distance from the model front surface, z. Note that the data were taken along the different crack path directions depending on the orientation of the slip plane, which will be discussed in the following section. Here, the slip plane activities are highly concentrated at the crack tip and decrease with an increase in the distance r. Magnitudes of γ^i_{SPA} are significantly different in the four different slip planes, indicating that the activations of each slip plane are not equivalent. It can be seen that γ^i_{SPA} generally converge to zero within r < 0.10 mm. The fatigue damage parameter F^i in Eq. (11) is calculated by integrating γ^i_{SPA} along r for each increment in the direction z. The integration should be carried out starting from the crack tip until γ^i_{SPA} reach zero. The fatigue damage parameter F^i along the specimen thickness can be obtained in this manner.

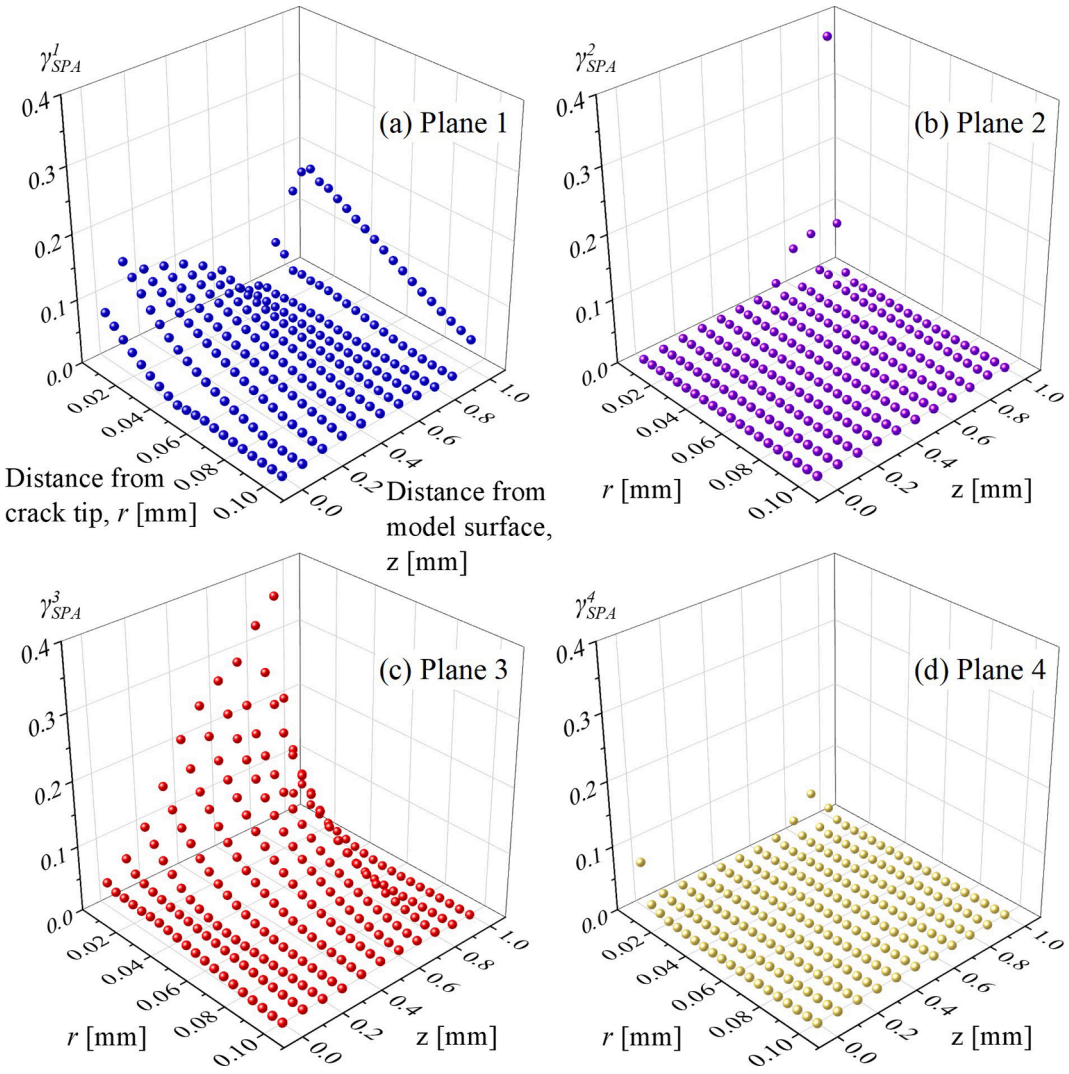

Fig. 10. Relationship between slip plane activity γ^i_{SPA} along the distance from the crack tip r and distance from the model surface z (⟨100⟩⟨100⟩ model, $\Delta K_I = 10$ MPa·m$^{1/2}$).

4.3. Numerical results of crystal plasticity analysis

The analytical results for the fatigue damage parameters F along the specimen thickness in the four models are summarized in Fig. 11. The applied loading is $\Delta K_I = 10$ MPa·m$^{1/2}$ for all models. Crack propagation along the crystallographic slip planes in each specimen may lead to different crack paths, as shown in Fig. 11. In the ⟨100⟩⟨100⟩ model, the damage parameter F was highest in slip plane 1 on the specimen front surface through the model thickness until the middle of the model, whereas F was highest in slip plane 3 from the middle of the model onward. Nevertheless, the average value of the damage parameter F in slip plane 1 is higher than that in slip plane 3. This indicates that the crack will mainly propagate along slip plane 1 and can easily deflect from slip plane 1 to slip plane 3 on the backside half of the specimen, which corresponds to the actual crack propagation in the experiment, as shown in Fig. 4(a). This deflection behavior in the ⟨100⟩⟨100⟩ specimen has also been observed in the ΔK increasing test in previous studies [14,16]. Notably, data from the node at the free surface should be omitted because they can lead to the generation of distorted elements, causing inaccurate analytical values. In the ⟨100⟩⟨110⟩ model, the activation of slip plane 1 is remarkably higher compared with the other slip planes. This result indicates that the crack will propagate along plane 1 without deflection. In fact, the ⟨100⟩⟨110⟩ specimen exhibited remarkably straight crack propagation along the blue slip plane, as shown in Fig. 4(b). In the ⟨110⟩⟨100⟩ model, the fatigue damage parameters F in all slip planes are comparable, which leads to multiple slips as discussed earlier. According to Chen et al. [12], the fatigue damage based on the slip deformation on the most activated slip plane should reach its critical point in order to initiate the transition from Mode I cracking to crystallographic cracking. Since the magnitudes of the F values in the ⟨110⟩⟨100⟩ model are significantly lower compared to the other models, it is possible that the F values could not reach their critical point, resulting in the Mode I propagation as revealed in the macroscopic and microscopic observation shown in Fig. 4(c) and Fig. 5(b), respectively. Finally, in the ⟨110⟩⟨110⟩ model, the F values in slip plane 1 are larger than those in the other slip planes in the vicinity of the model surface. However, the F values in all slip planes are comparable around the center of the model, which leads to the activation of other slip planes. This numerical result correlates well with the crack propagation path in the experiment, as shown in Fig. 4(d), where multiple crack planes can be observed, particularly at the center of the specimen.

To compare the fatigue damage at the near-threshold regime, the highest damage parameters F among the four slip planes in each model were averaged along the thickness by omitting data at the surface. The average values of F, calculated for various values of ΔK_I in the loading range corresponding to the experimental conditions, are plotted as a function of ΔK_I in Fig. 12. Fig. 12(a) shows their relationship in both the near-threshold regime as well as in higher loading regime, where Fig. 12(b) only shows the data in the near-threshold regime from the ΔK_I decreasing test. The open symbols indicate the results corresponding to ΔK_{th} in each specimen. In the ⟨100⟩⟨100⟩, ⟨100⟩⟨110⟩, and ⟨110⟩⟨110⟩ specimens, the average damage parameters F at ΔK_{th} are almost comparable at approximately $F = 2$ μm. The reason for this is that the resistance for crystallographic cracking is related to the intrinsic slip property of the FCC crystal rather than the crystallographic orientation of the specimen.

As shown in Fig. 12, the F values in the ⟨110⟩⟨100⟩ specimens are remarkably lower compared with the other three models. Additionally, the magnitudes of these F values are approximately equivalent, as shown in Fig. 11(c). These two situations caused Mode I crack propagation, unlike the other three models discussed earlier. To rationalize the crack propagation rate and ΔK_{th} of Mode I cracking associated with the multiple slip mechanism, the damage parameter should be evaluated by considering the activation of all slip systems. The damage parameter is given as follows:

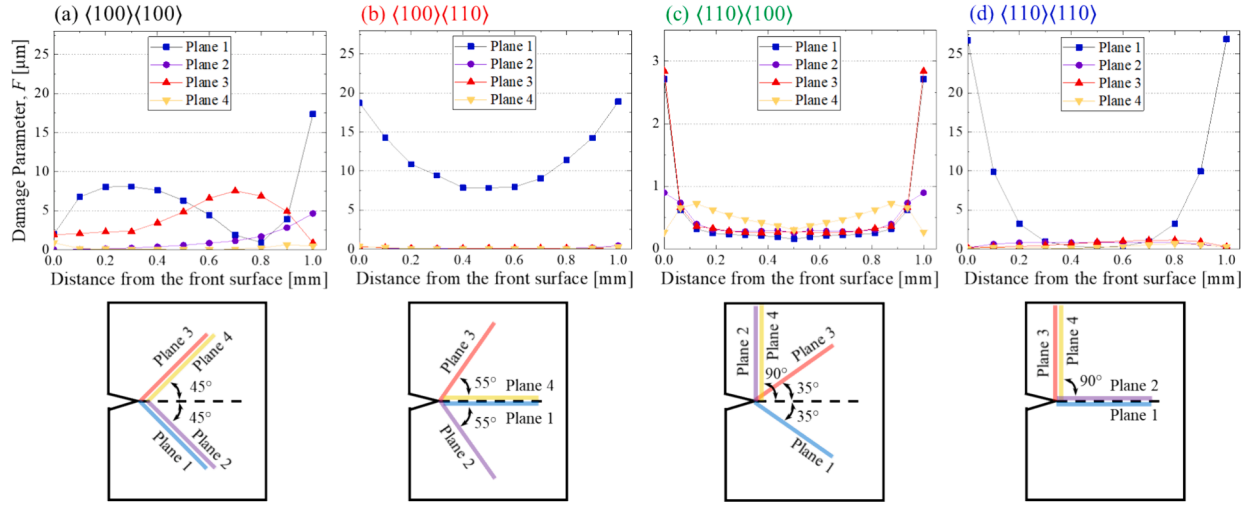

Fig. 11. Analytical results of fatigue damage parameter F where $\Delta K_I = 10$ MPa·m$^{1/2}$ for (a) ⟨100⟩⟨100⟩, (b) ⟨100⟩⟨110⟩, (c) ⟨110⟩⟨100⟩, and (d) ⟨110⟩⟨110⟩ models. The illustrations show the crack path direction along four crystallographic slip planes, which are different in each model.

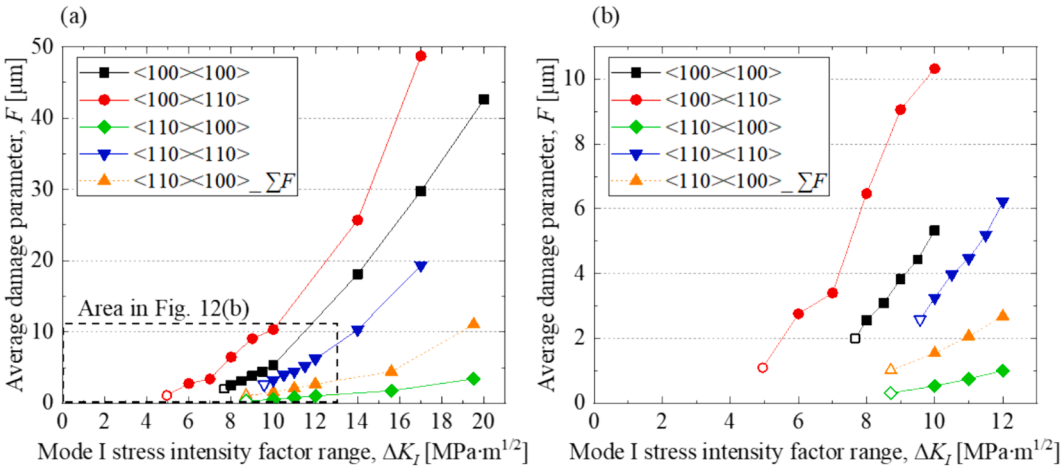

Fig. 12. Relationship between ΔK_I and average values of F along specimen thickness for (a) in the near-threshold regime and higher loading regime and (b) only in the near-threshold regime. The dashed line in the ⟨110⟩⟨100⟩ specimen indicates the F value calculated by summation among the four crystallographic slip planes.

$$\sum F = \sum_{i=1}^{4} F^i, \tag{13}$$

where F^i is the same as that in Eq. (11). This ΣF considers the contribution of the slip plane activities of all 4 slip planes as the activation of all 4 slip planes should contribute to Mode I cracking. This concept also corresponds to the crack advancing model proposed by Antolovich et al. [41], which correlates crack propagation with the slip bands intersecting the plane normal to the loading direction.

The computed results of ΣF in the ⟨110⟩⟨100⟩ model are indicated by the orange dashed line in the plot shown in Fig. 12. As can be seen, the values of ΣF in the ⟨110⟩⟨100⟩ model approach the average values of F in the other three models. Notably, the values of F in the ⟨110⟩⟨100⟩ model do not increase significantly with a certain increase in ΔK_I compared with the other three models. The reason for this is that the resistances to the crystallographic cracking and Mode I cracking are different. Nevertheless, it is necessary to consider the term F in Mode I cracking and crystallographic cracking simultaneously instead of considering only ΔK_I, which does not consider elastic anisotropy.

Fig. 13 shows the relationship between the experimental da/dN from both ΔK_I decreasing and ΔK_I increasing tests and computed average values of F along the specimen thickness for all specimens. The ΣF is used in the plot for the ⟨110⟩⟨100⟩ specimen. As can be seen, all data of the four different crystallographic orientations exhibit a similar trend, where a higher experimental da/dN value results in a higher average damage parameter F. This trend is similar to the results obtained at higher temperature [12]. Therefore, the fatigue crack propagation rate in crystallographic cracking and Mode I cracking can be evaluated regardless of the crystallographic orientation using the damage parameters F and ΣF, respectively.

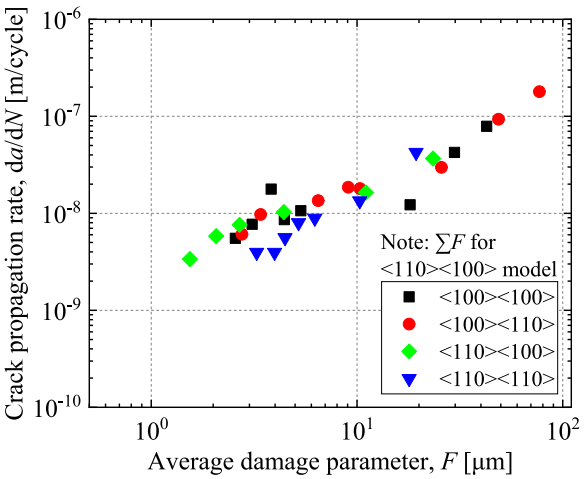

Fig. 13. Relationship between experimental crack propagation rate and computed average values of F along specimen thickness.

Lastly, it should be noted that the current FE model shown in Fig. 9 did not accurately replicate the crack paths of the actual cracks observed in the experiment. The presence or absence of multiple crack tips and deflection behavior might affect an effective driving force for the crack propagation. Although this might not significantly affect the results in Fig. 13, this should be considered for more precise simulations in future studies. Also, the resistances to the crystallographic cracking and Mode I cracking are different, which is probably a factor contributing to the gap between the plot of the ⟨110⟩⟨100⟩ specimen and the other three specimens. Such different resistances should be further verified. In addition, the crystal plasticity constitutive equation employed in this study does not take into account cyclic hardening and softening. Although the cyclic hardening and softening may not significantly affect the main conclusions regarding the influence of the crystallographic orientations, such factors may also exhibit different behaviors depending on the crystallographic orientations; thus, further detailed investigation is necessary.

5. Conclusions

This study conducted experimental and numerical investigations to elucidate the fatigue crack propagation behavior in the near-threshold regime in a single crystal Ni-based superalloy with different crystallographic orientations. Fatigue tests were conducted on four specimen types with different crystallographic orientations at room temperature. Additionally, crystal plasticity finite element analyses were conducted to investigate the plastic deformation (slip) of an octahedral slip system in front of the crack tip, with consideration to the actual 3D geometry of the crack tip and elastic anisotropy. The following conclusions were drawn:

1. Fatigue tests revealed that crystallographic orientation significantly affects the fatigue crack propagation behavior. The fatigue cracks exhibited mixed-mode propagation encompassing Mode I, II, and III propagation along the crystallographic slip planes in the ⟨100⟩⟨100⟩, ⟨100⟩⟨110⟩, and ⟨110⟩⟨110⟩ specimens, while Mode I cracking occurred in the ⟨110⟩⟨100⟩ specimen. The configuration of the crystallographic slip planes was found to be one of the dominant factors affecting the fatigue crack propagation rate. Additionally, the fatigue thresholds were different, depending on the specimens' crystallographic orientation.
2. A damage parameter, which accounts for the fatigue damage on the individual slip plane, offers a valuable approach to understanding the fatigue crack propagation behavior in the near-threshold regime for the material used. This parameter has shown potential in rationalizing the crack propagation paths and rates in the experiments and capturing the influence of crystallographic orientation on fatigue threshold.

CRediT authorship contribution statement

Putt Thanakun: Writing – original draft, Validation, Methodology, Investigation, Formal analysis. **Itsuki Sasakura:** Methodology, Investigation, Data curation, Conceptualization. **Keita Mase:** Methodology, Data curation, Conceptualization. **Motoki Sakaguchi:** Writing – review & editing, Supervision, Project administration, Funding acquisition, Conceptualization.

Declaration of competing interest

The authors declare that they have no known competing financial interests or personal relationships that could have appeared to influence the work reported in this paper.

Data availability

Data will be made available on request.

Acknowledgements

We thank Edanz (https://jp.edanz.com/ac) for editing a draft of this manuscript.

References

[1] Cowles BA. High cycle fatigue in aircraft gas turbines—an industry perspective. Int J Fract 1996;80:147–63. https://doi.org/10.1007/BF00012667.
[2] Hicks MA, King JE. Temperature effects on fatigue thresholds and structure sensitive crack growth in a nickel-base superalloy. Int J Fatigue 1983;5:67–74. https://doi.org/10.1016/0142-1123(83)90056-7.
[3] King JE. Fatigue crack propagation in nickel-base superalloys – effects of microstructure, load ratio, and temperature. Mater Sci Technol 1987;3:750–64. https://doi.org/10.1179/026708387790329766.
[4] Mercer C, Soboyejo ABO, Soboyejo WO. Micromechanisms of fatigue crack growth in a forged Inconel 718 nickel-based superalloy. Mater Sci Eng A 1999;270:308–22. https://doi.org/10.1016/S0921-5093(99)00214-2.
[5] Arakere NK, Swanson G. Effect of crystal orientation on fatigue failure of single crystal nickel base turbine blade superalloys. J Eng Gas Turbines Power 2002;124:161–76. https://doi.org/10.1115/1.1413767.
[6] Li B, Rosa LG. Prediction models of intrinsic fatigue threshold in metal alloys examined by experimental data. Int J Fatigue 2016;82:616–23. https://doi.org/10.1016/j.ijfatigue.2015.09.018.
[7] Zerbst U, Vormwald M, Pippan R, Gänser HP, Sarrazin-Baudoux C, Madia M. About the fatigue crack propagation threshold of metals as a design criterion – A review. Eng Fract Mech 2016;153:190–243. https://doi.org/10.1016/j.engfracmech.2015.12.002.
[8] Chen B, Jiang J, Dunne FPE. Microstructurally-sensitive fatigue crack nucleation in Ni-based single and oligo crystals. J Mech Phys Solids 2017;106:15–33. https://doi.org/10.1016/j.jmps.2017.05.012.

[9] Suzuki S, Sakaguchi M, Inoue H. Temperature dependent fatigue crack propagation in a single crystal Ni-base superalloy affected by primary and secondary orientations. Mater Sci Eng A 2018;724:559–65. https://doi.org/10.1016/j.msea.2018.03.090.

[10] Chen B, Jiang J, Dunne FPE. Is stored energy density the primary meso-scale mechanistic driver for fatigue crack nucleation? Int J Plast 2018;101:213–29. https://doi.org/10.1016/j.ijplas.2017.11.005.

[11] Sakaguchi M, Komamura R, Chen X, Higaki M, Inoue H. Crystal plasticity assessment of crystallographic Stage I crack propagation in a Ni-based single crystal superalloy. Int J Fatigue 2019;123:10–21. https://doi.org/10.1016/j.ijfatigue.2019.02.003.

[12] Chen X, Sakaguchi M. Transition behavior from Mode I cracking to crystallographic cracking in a Ni-base single crystal superalloy. Int J Fatigue 2020;132:105400. https://doi.org/10.1016/j.ijfatigue.2019.105400.

[13] Suzuki S, Sakaguchi M. Fatigue crack retardation associated with creep deformation induced by a tension hold in a single crystal Ni-base superalloy. Scr Mater 2020;178:346–50. https://doi.org/10.1016/j.scriptamat.2019.11.058.

[14] Okamoto R, Suzuki S, Sakaguchi M, Inoue H. Evolution of short-term creep strain field near fatigue crack in single crystal Ni-based superalloy measured by digital image correlation. Int J Fatigue 2022;162:106952. https://doi.org/10.1016/j.ijfatigue.2022.106952.

[15] Sakaguchi M, Okamoto R, Karato T, Suzuki K. Effect of rafted microstructure and its temperature dependency on fatigue crack propagation in a single-crystal Ni-base superalloy. Fatigue Fract Eng Mater Struct 2023;46:590–602. https://doi.org/10.1111/ffe.13888.

[16] Chen X, Hu D, Sakaguchi M. Temperature dependent transition from Mode I to crystallographic cracking in a Ni-base single crystal superalloy. Theor Appl Fract Mech 2023;124:103795. https://doi.org/10.1016/j.ijfatigue.2019.105400.

[17] Zhai T, Wilkinson AJ, Martin JW. A Crystallographic mechanism for fatigue crack propagation through grain boundaries. Acta Mater 2000;48:4917–27. https://doi.org/10.1016/S1359-6454(00)00214-7.

[18] Gao Y, Stölken JS, Kumar M, Ritchie RO. High-cycle fatigue of nickel-base superalloy René 104 (ME3): Interaction of microstructurally small cracks with grain boundaries of known character. Acta Mater 2007;55:3155–67. https://doi.org/10.1016/j.actamat.2007.01.033.

[19] Kumar S, Curtin WA. ack interaction with microstructure. Mater Today 2007;10:34–44. https://doi.org/10.1016/S1369-7021(07)70207-9.

[20] Sengupta A, Putatunda SK. Kinetics of γ' precipitation and its influence on fatigue crack growth behavior of a new single-crystal nickel-based superalloy (CMSX-4G) at room temperature. J Mater Eng Perform 1993;2:57–68. https://doi.org/10.1007/BF02649675.

[21] Sengupta A, Putatunda SK, Balogh M. Fatigue crack growth behavior of a new single crystal nickel-based superalloy (CMSX-4) at 650 °C. J Mater Eng Perform 1994;3:540–50. https://doi.org/10.1007/BF02645320.

[22] Pang HT, Reed PAS. Microstructure variation effects on room temperature fatigue threshold and crack propagation in Udimet 720Li Ni-base superalloy. Fatigue Fract Eng Mater Struct 2009;32:685–701. https://doi.org/10.1111/j.1460-2695.2009.01366.x.

[23] Telesman J, Smith TM, Gabb TP, Ring AJ. Relationship between unusual high-temperature fatigue crack growth threshold behavior in superalloys and sudden failure mode transitions. Mater Sci Eng A 2017;708:336–50. https://doi.org/10.1016/j.msea.2017.10.003.

[24] He Y, Li W, Yang M, Zhao Z, Zhang X, Dong P, et al. A theoretical model for predicting the temperature-dependent fatigue crack propagation threshold of nickel-based superalloys. Theor Appl Fract Mech 2022;118:103248. https://doi.org/10.1016/j.tafmec.2022.103248.

[25] Wan VVC, Maclachlan DW, Dunne FPE. A stored energy criterion for fatigue crack nucleation in polycrystals. Int J Fatigue 2014;68:90–102. https://doi.org/10.1016/j.ijfatigue.2014.06.001.

[26] Karamitros V, MacLachlan DW, Dunne FPE. Modelling of short crack growth in single crystal Ni $\gamma-\gamma'$ microstructure. Acta Mater 2022;240:118305. https://doi.org/10.1016/j.actamat.2022.118305.

[27] Karamitros V, MacLachlan DW, Dunne FPE. Mechanistic fatigue in Ni-based superalloy single crystals: A study of crack paths and growth rates. J Mech Phys Solids 2022;158:104663. https://doi.org/10.1016/j.jmps.2021.104663.

[28] MacLachlan DW, Karamitros V, Dunne FPE. Mechanistic modelling of fatigue nucleation and short crack growth in polycrystalline alloys. J Mech Phys Solids 2023;177:105314. https://doi.org/10.1016/j.jmps.2023.105314.

[29] Sakaguchi M, Thanakun P, Koshio A, Tokihiro K, Inoue H. Temperature change and fatigue crack initiation associated with local cyclic slip deformation in a single crystal material. Fatigue Fract Eng Mater Struct 2023;46:4486–97. https://doi.org/10.1111/ffe.14146.

[30] Standard Test Method for Measurement of Fatigue Crack Growth Rates. Annual Book ASTM standards E647-22. ASTM Int 2023;52–13.

[31] Forsyth PJE. A two stage process of fatigue crack growth. Proc Crack Propagation Symposium 1962.

[32] Meggiolaro MA, Miranda ACO, Castro JTP, Martha LF. Stress intensity factor equations for branched crack growth. Eng Fract Mech 2005;72:2647–71. https://doi.org/10.1016/j.engfracmech.2005.05.004.

[33] Kitagawa H, Yuuki R, Ohira T. Crack-morphological aspects in fracture mechanics. Eng Fract Mech 1975:7. https://doi.org/10.1016/0013-7944(75)90052-1.

[34] Sakaguchi M, Tsuru T, Okazaki M. Fatigue crack propagation in thin-wall superalloys component; experimental investigation via miniature CT specimen. Superalloys 2012;2012:431–7. https://doi.org/10.1002/9781118516430.ch47.

[35] Asaro RJ. Crystal plasticity. J Appl Mech 1983;50:921–34. https://doi.org/10.3390/cryst11010044.

[36] Zhang H, Li P, Gong X, Wang T, Li L, Liu Y, et al. Tensile properties, strain rate sensitivity and failure mechanism of single crystal superalloys CMSX-4. Mater Sci Eng A 2020;782:139105. https://doi.org/10.1016/j.msea.2020.139105.

[37] Lan W, Deng X, Sutton MA. Investigation of crack tunneling in ductile materials. Eng Fract Mech 2010;77:2800–12. https://doi.org/10.1016/j.engfracmech.2010.06.010.

[38] Siebörger D, Knake H, Glatzel U. Temperature dependence of the elastic moduli of the nickel-base superalloy CMSX-4 and its isolated phases. Mater Sci Eng A 2001;298:26–33. https://doi.org/10.1016/s0921-5093(00)01318-6.

[39] Fatemi A, Socie DF. A critical plane approach to multiaxial fatigue damage including out-of-phase loading. Fatigue Fract Eng Mater Struct 1988;11:149–65. https://doi.org/10.1111/j.1460-2695.1988.tb01169.x.

[40] Sakaguchi M, Komamura R, Hosaka Y, Inoue H. Stage i fatigue crack propagation in a single crystal and a directional solidified Ni-base superalloy. Proc Int Symp Superalloys 2016;2016-January:639–46. 10.1002/9781119075646.ch68.

[41] Antolovich BF, Saxena A, Antolovich SD. Fatigue crack propagation in single-crystal CMSX- 2 at elevated temperature. J Mater Eng Perform 1993;2:489–95. https://doi.org/10.1007/BF02661731.